Proceedings of ASME Turbo Expo 2020: Turbomachinery Technical Conference and Exposition
GT2020
June 22-26, 2020, London, United Kingdom

GT2020-15008

LOAD INFLUENCE ON HYDROSTATIC OIL FILM JOURNAL BEARING STIFFNESS CHARACTERISTICS

Leonid Moroz, Leonid Romanenko, Roman Kochurov, Evgen Kashtanov

SoftInWay, Inc.
1500 District Ave, Burlington, MA 01803, USA

ABSTRACT

Hydrostatic bearings are widely used in industry, including aerospace and energy sectors. Hydrodynamic lubrication mechanism has been well studied analytically and experimentally and various types of bearings were developed to provide increasing operating speed, load capacity, stability and efficiency for modern rotating machines. Hydrostatically lubricated bearings have principal difference (in comparison with hydrodynamic bearings) and their characteristics have been an area of continued research.

The goal of this work is to develop a robust algorithm, which can predict hydrodynamical characteristics and dynamic stiffness and damping coefficients of hybrid and hydrostatic bearings with increased accuracy and which can be used for engineering/design purposes. The developed approach is based on Reynold's equations, where the unknown parameters are the rotor position and fluid pressure in recess pockets. Finite difference method in combination with the successive over-relaxation algorithm is used for a numerical solution of Reynold's equations. Newton's method is applied to solve the generated system of equations.

Applying the developed approach, the effect of load influence on the hydrodynamical and the dynamic stiffness characteristics has been studied. Several hydrostatic bearing designs which are based on the published data were considered to compare the results calculated applying the approach with the experimental and theoretical data given in the literature. Performed study shows when journal eccentricity can't be neglected while simulating hydrostatic bearing characteristics. Simulations also allow for analysis of how different design/geometrical parameters and initial conditions (supply pressure) influence bearing performance characteristics.

The developed approach can be utilized as a practical tool which allows for the prediction of performance characteristics of hydrostatic bearing with increased accuracy.

Keywords: hydrostatic bearing, oil film, journal, dynamic coefficients, stiffness, damping, eccentricity.

INTRODUCTION

Hydrostatic and hybrid oil film journal bearings have been widely used in various rotating machinery applications because of their unique features. The main advantages of hydrostatic bearings are long life without wear (because they have lift at zero speed and an almost constant oil film thickness vs. rotor speed), high load carrying capacity, large fluid film stiffness and damping capacity. Fluid viscosity has no effect on hydrostatic bearings load capacity nor static stiffness. Because of this feature hydrostatic bearings can be used for application with non-viscous fluids such as gases or cryogenic fluids. Hydrostatic bearing design contains an external pressure supply system, which forms the high pressure in the bearing to support journal at high loads and low shaft rotation speeds. The complexity of the pressurized lubrication system is one major disadvantage of the bearing design. Other drawbacks are the necessity for installation of axillary equipment for oil filtration and control, high power consumption because of pumping losses, and potential instabilities at operation in 'hybrid' mode, etc. There are two types of hydrostatic bearings, depending on the fluid supply system: flow-constant and pressure constant (contain a restrictor such as an orifice or a capillary).

Hydrostatic bearings have been investigated by numerous researchers. Review of articles about hydrostatic bearings from 1990 to 2016 is presented in [1]. Reference [1] shows an overview of different methods including governing equations and solution processes that are used to describe hydrostatic bearing fluid dynamics. Complete Navier-Stokes equations are utilized by many authors to simulate the flow in a hydrostatic bearing pockets and obtain a good agreement with experimental results [2], [3]. This approach requires significant computational resources and pre-processor work and can be applied for a specific design only.

Another approach is to use Reynold's equations which derive from Navier-Stokes equations with some assumptions (neglecting the transversal velocity, constant pressure across the film thickness, etc). Experimental pressure distribution measurements in hybrid journal bearings are performed and compared with theoretical results in [4]. An influence of inertia forces in the recess outlets and pressure generation in the pockets for high rotating speeds are shown. In [4] theoretical calculations were based on modified Reynold's equations, given by Constantinescu equations[5]. The usual methods for solving Reynold's equations and calculating static and dynamic performance parameters are finite difference method (FDM) [6], finite element method (FEM) [7], etc.

Based on the review it can be concluded that effects of turbulence, compressibility in the fluid film, inertia, and thermal effects have an influence on hydrostatic bearing performance and need to be accounted. Often, further simplifications for the Reynolds equations are used. For example, assuming zero eccentricity for the shaft sometimes leads to inaccuracy in predicted hydrodynamic characteristics.

In the current article, an improved methodology has been developed for hydrodynamic and mechanical characteristics of hybrid and hydrostatic bearings simulation, which allows to increase accuracy for the results. In the proposed methodology, models for journal bearing film thickness depending on the shaft position and for fluid flow through the bearing are established. Shaft equilibrium position and flow through restrictors (orifice or capillary) are then determined based on the applied bearing load (inverse problem). Fluid influence is modeled as stiffness added to the shaft and shaft equilibrium position which is determined during the iterative solution process. Pressures in the recess chambers depends on the flow through the restrictor, and the flow depends on the shaft position.

Advantages of the developed approach are the following:

1) Accurate simulation for the shaft equilibrium position depending on the applied load and correct determination for pressure and flow rates in the restrictors. The position of the shaft influences restrictor flow rates and pressures;
2) Shaft vibrations influence the pressure in recess chambers. These pressure variations have been included in calculations for the damping coefficients.

Several hydrostatic bearing designs based on published data were used to compare the results calculated applying the approach with the experimental and theoretical data given in the literature.

The effect of eccentricity influence is demonstrated in Fig. 1, where a typical hydrostatic bearing is shown. When a journal operates in the center of the hydrostatic bearing, pressures and flow rates in the recess chambers are almost the same. Due to journal displacement with some eccentricity, pressures in recess chambers become different. The pressures in recess chambers #1 and #4 become higher because of the smaller gap between chambers and shaft, while pressures in chambers #2 and #3 become lower due to higher gap. Flow rates through chambers are also changed – now with more flow passing through chambers #2 and #3.

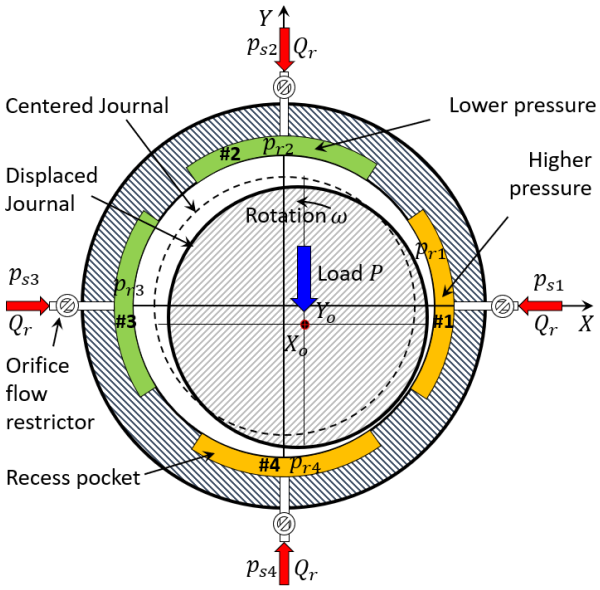

Figure 1: Typical Hydrostatic Bearing

Thus, pressure distribution within a hydrostatic bearing is influenced by a nonuniform gap between journal and chambers walls. The change of pressures in the recess chambers results in changes of bearing dynamic characteristics.

The focus of the study is to show how hydrostatic bearing characteristics depend on the applied load and shaft eccentricity and determine conditions when inclusion of eccentricity effect is mandatory.

NOMENCLATURE

FDM – finite difference method;
FEM – finite element method;
SOR – successive over-relaxation;

Symbols

A_{oi} – the orifice area, m^2;
$d\beta$ – recess length (circumferential), *deg*;
C_{di} – orifice flow ration coefficient;
C_b – bearing radial clearance, *m*;
c_{xx}, c_{xy}, c_{yx}, c_{yy} – bearing's damping coefficients, *N·s/m*;
D – journal bearing diameter, *m*;
d_{oi} – orifice diameter, *m*;
d_{ci} – capillary diameter, *m*;
G_x – turbulent flow coefficient (circumferential direction);
G_y – turbulent flow coefficient (axial direction);
F_x, F_y – reaction forces acting on the shaft from oil film (x-, y- components), *N*;
h – oil film thickness function, *m*;
h_r – recess thickness, *m*;
L – bearing effective length, *m*;
L_r – recess length (axial), *m*;
k_{xx}, k_{xy}, k_{yx}, k_{yy} – bearing's stiffness coefficients, *N/m*;

l_i – the length of the capillary tube, *m*;
n – number of recess chambers;
p – fluid film hydrodynamic gauge pressure, *Pa*;
p_{si} – oil supply pressure, *Pa*;
p_{ri} – oil supply pressure in recess, *Pa*;
P – journal load, *N*;
P_x, P_y – journal load (x-, y- components), *N*;
Q_{oi}, Q_{ci} – flow rate for an orifice or capillary feeding, m^3;
Re – Reynolds number;
U – surface velocity, *m/s*;
U_1 – journal to bearing surface velocity, *m/s*;
u – velocity in circumferential direction, *m/s*;
v – velocity in axial direction, *m/s*;
v_n – fluid velocity component normal to the contour, *m/s*;
v_x – velocity of the journal center, X- component;
v_y – velocity of the journal center, Y- component;
w – velocity along film thickness, *m/s*;
X – horizontal axis (shaft coordinate system);
Y – vertical axis (shaft coordinate system);
X_0 – journal center X-coordinate, *m*;
Y_0 – journal center Y-coordinate, *m*;
x – axis in circumferential direction;
y – axis in axial direction;
z – axis along film thickness;
ρ – fluid density, kg/m^3;
θ – fluid fraction variable;
μ – fluid dynamic viscosity, *Pa·s*;
φ – angular coordinate;
ω – shaft rotational speed, *rad/s*;
Ω – non-dimensional computational domain;
Ω^+ – the pressurized region of the bearing;
Ω_0 – cavitated region;
Ω_r – recess region;
$\sum$ – cavitation boundary (between Ω^+ and Ω_0);
Γ_0 – outlet boundary;
Γ_a – feeding boundary.

1. PROBLEM FORMULATION AND METHODOLOGY DESCRIPTION

Typical hydrostatic bearing shown in Fig. 1 is considered. Initial parameters for the analysis are

1) Bearing geometry,
2) Shaft (journal) rotational speed,
3) Oil supply pressure,
4) Liquid properties, and
5) Journal load.

The task is to determine journal equilibrium position at steady state operation (X, Y coordinates of the journal center), fluid flow rates and pressures in recess chambers. Bearing stiffness and damping coefficients shall be determined also based on hydrodynamic characteristics.

The parameters listed above satisfy a system of $(2 + n)$ nonlinear equations which consists of 2 equations of journal equilibrium position and n equations which describe relations between pressures and flow rates in recess chambers.

Equations for journal equilibrium position determination are presented in the form (1):

$$\begin{aligned} P_x + F_x &= 0; \\ P_y + F_y &= 0, \end{aligned} \tag{1}$$

where P_x, P_y – journal load (x-, y- components), F_x, F_y – reaction forces acting on the shaft from oil film (x-, y- components).

Formulas for a film flow are derived from Navier-Stokes equations [10] and describe velocity distribution in the film (see Fig. 2):

$$u = \frac{1}{2\mu}\frac{\partial p}{\partial x}(z^2 - zh) + \left(1 - \frac{z}{h}\right)U_1; \tag{2}$$

$$v = \frac{1}{2\mu}\frac{\partial p}{\partial y}(z^2 - zh), \tag{3}$$

where u – velocity corresponds to an axis x (circumferential direction); v – velocity corresponds to an axis y (axial direction); U_1 represents the velocity of the rotor surfaces.

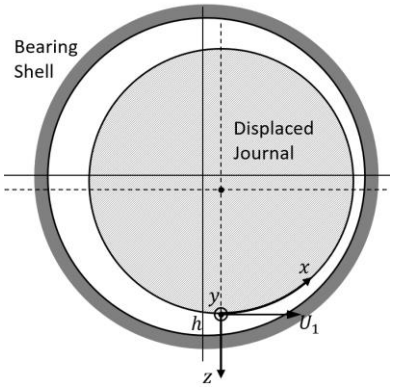

Figure 2: Bearing Surfaces Coordinate Axes

According the proposed approach, fluid dynamics is described by the mass-conserving mathematical model proposed by Elrod & Adams [8, 9]. It is well-established as an accurate tool for simulation of the hydrodynamic/hydrostatic lubrication including cavitation. Additional modifications to account for turbulent flow were incorporated into the model. For hydrostatic and hybrid bearings pressure drop at the recess pocket boundary due to the narrowing of the channel have been taken into the account. The model involve calculation of two fields: p is hydrodynamic pressure and θ is a fluid fraction variable, which takes values between zero and one. The governing equations are presented in the form (4), where the problem is formulated for hydrodynamic bearing with gap thickness $h(x, y, t)$.

$$\frac{\partial}{\partial x}\left(G_x\frac{h^3}{\mu}\frac{\partial p}{\partial x}\right) + \frac{\partial}{\partial y}\left(G_y\frac{h^3}{\mu}\frac{\partial p}{\partial y}\right) = \frac{U_1(t)}{2}\frac{\partial h\theta}{\partial x} + \frac{\partial h\theta}{\partial t} \quad in\ \Omega\backslash\Sigma. \tag{4}$$

The x-axis is chosen parallel to the sliding velocity (in bearing's circumferential direction), y-axis is chosen in axial direction (see Fig. 2). Computational domain Ω is assumed to be a rectangle in the (x, y) coordinates. G_x and G_y are the turbulent flow coefficients in circumferential and axial direction correspondingly, which are correction factors of viscosity caused by the turbulent diffusion. For turbulent flow these coefficients are calculated by formulas (5), (6):

$$G_x = \frac{1}{12 + 0.0136Re^{0.90}}; \tag{5}$$

$$G_y = \frac{1}{12 + 0.0043Re^{0.96}}, \tag{6}$$

where local Reynolds number can be calculated as:

$$Re = \frac{\rho U_1 h}{\mu}. \tag{7}$$

For laminar flow $G_x = G_y = 1/12$.

Boundary conditions are described by formulas (8):

$$\begin{gathered} p \geq 0, \quad \theta = 1 \quad in \quad \Omega^+; \\ p = 0, \quad \theta < 1 \quad in \quad \Omega_0; \\ p = 0, \quad on \quad \sum; \\ p = p_{si}, \quad on \quad \Gamma_{si}; \\ p = p_{ri}, \quad in \quad \Omega_r. \end{gathered} \tag{8}$$

The numerical solution of equation (4) is generated using finite difference method with successive over-relaxation (SOR) algorithm.

Forces acting on the rotor from the fluid are described by following formulas:

$$\begin{Bmatrix} F_x \\ F_y \end{Bmatrix} = \int_0^L \int_0^{2\pi} P \begin{Bmatrix} \cos\varphi \\ \sin\varphi \end{Bmatrix} d\varphi dy. \tag{9}$$

Flow rates through recess chambers can be determined by formula [10]:

$$Q_{ri} = \oint_{d\Gamma_i} v_n h dl, \tag{10}$$

where v_n is fluid velocity component normal to the contour Γ and can be described as:

$$v_n = \bar{u} \;\; n_x + \bar{v} \;\; n_y, \tag{11}$$

where n_x, n_y – projections of normal vector on x- and y-axis correspondingly, $\bar{u}$, $\bar{v}$ – averaged by thickness velocity along x- and y-axis correspondingly.

Recess pressures in chambers depend on a flow rate through a fluid restrictor. The flow rate Q_{ri} can be written as a function of a pressure drop:

$$Q_{ri} = Q_{oi} = A_{oi} C_{di} \sqrt{\frac{2}{\rho}(p_{si} - p_{ri})}; \tag{12}$$

$$Q_{ri} = Q_{ci} = \frac{\pi \cdot {d_{ci}}^4}{128 \cdot \mu \cdot l_{ci}}(p_{si} - p_{ri}), \tag{13}$$

where Q_{oi} is the flow rate through the orifice and Q_{ci} is the flow rate for a capillary feeding type of restrictor. For a simplicity of material presentation, the orifice type will be considered in the article. In the case of capillary type of restrictor, the approach will be the same.

A system of $(2 + n)$ nonlinear equations, where unknown parameters are rotor position (X_o, Y_o), and pressures in recess chambers p_{ri} is solved by Newton-Raphson method. Algorithm of the solution process is presented in Fig. 3.

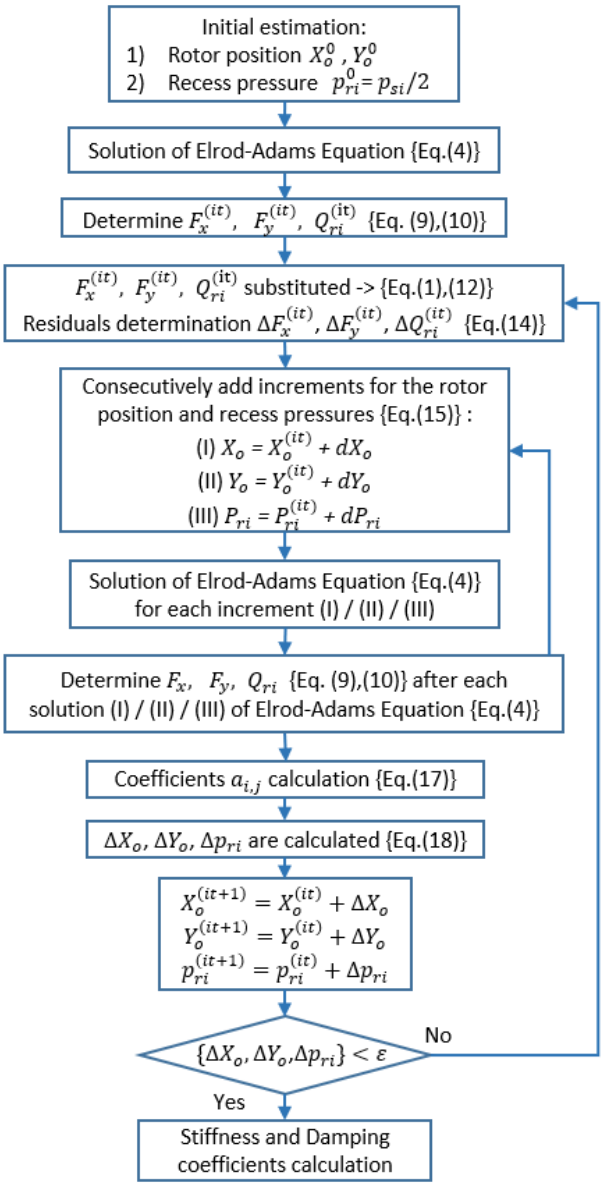

Figure 3: Analysis Flow Chart

At the first step of the solution process an initial estimation of the rotor journal equilibrium position (X_o^0, Y_o^0) and recess pressure in pockets p_{ri}^0 ($p_{ri}^0 = p_{si}/2$) are selected. Elrod-Adams equation (4) is solved and fluid film thickness h, pressure distribution p, and fluid fraction variable θ are calculated. Forces $F_x^{(it)}$, $F_y^{(it)}$ and flow rates $Q_{ri}^{(\mathrm{it})}$ can be determined from equations (9), (10). Symbol ' $^{(it)}$' corresponds to the current iteration. $F_x^{(it)}$, $F_y^{(it)}$, $Q_{ri}^{(\mathrm{it})}$ are then substituted in equilibrium equations (1) and equation for flow rates calculation (12) to determine residuals $\Delta F_x^{(it)}$, $\Delta F_y^{(it)}$ by following formulas:

$$\begin{aligned} \Delta F_x^{(it)} &= P_x - F_x^{(it)}; \\ \Delta F_y^{(it)} &= P_y - F_y^{(it)}; \\ \Delta Q_{ri}^{(it)} &= \Delta Q_{ri}^{(it)} - A_{oi} C_{di} \sqrt{\frac{2}{\rho}(p_{si} - p_{ri})} \end{aligned} \tag{14}$$

One by one, increments for the rotor position and pressures in recess pockets determined by the formulas (15) are added and equation (4) is solved. Forces F_x, F_y and flow rate Q_{ri} are determined after each solution of Elrod-Adams equation.

$$\begin{aligned} X_o^{(it)} &= X_o^{(it)} + dX_o \; ; \\ Y_o^{(it)} &= Y_o^{(it)} + dY_o \; ; \\ p_{ri}^{(it)} &= p_{ri}^{(it)} + dp_{ri}. \end{aligned} \tag{15}$$

Increments for forces and flow rates depending on increments for rotor coordinates and flow pressures in recess chambers can be written in the form (16):

$$\begin{aligned} dF_x &= a_{1,1} dX_o + a_{1,2} dY_o + \sum_{i=1}^{n} \left(a_{1,2+i} dp_{ri}\right); \\ dF_y &= a_{2,1} dX_o + a_{2,2} dY_o + \sum_{i=1}^{n} \left(a_{2,2+i} dp_{ri}\right); \\ dQ_{rj} &= a_{j+2,1} dX_o + a_{j+2,2} dY_o + \sum_{i=1, i\neq j}^{n} \left(a_{j+2,i+2} dp_{ri}\right), \end{aligned} \tag{16}$$

where coefficients $a_{i,j}$ can be determined by formulas (17) at the next step of solution process

$$\begin{aligned} a_{1,1} &= \frac{\partial F_x}{\partial x}, a_{2,1} = \frac{\partial F_y}{\partial x}, a_{i+2,1} = \frac{\partial Q_{ri}}{\partial x}, \\ a_{1,2} &= \frac{\partial F_x}{\partial y}, a_{2,2} = \frac{\partial F_y}{\partial y}, a_{i+2,2} = \frac{\partial Q_{ri}}{\partial y}, \\ a_{1,j+2} &= \frac{\partial F_x}{\partial p_{rj}}, a_{2,j+2} = \frac{\partial F_y}{\partial p_{rj}}, a_{j+2,i+2} = \frac{\partial Q_{rj}}{\partial p_{ri}}, \end{aligned} \tag{17}$$

Derivatives from equations (17) are calculated numerically; ∂F_x, ∂F_y - difference between given and calculated (by integration) forces.

System of equations (18) is then constructed and solved with respect to increments ΔX_o, ΔY_o, Δp_{ri}.

$$\begin{aligned} \Delta F_x &= a_{1,1}\Delta X_o + a_{1,2}\Delta Y_o + \sum_{i=1}^{n} \left(a_{1,2+i}\Delta p_{ri}\right); \\ \Delta F_y &= a_{2,1}\Delta X_o + a_{2,2}\Delta Y_o + \sum_{i=1}^{n} \left(a_{2,2+i}\Delta p_{ri}\right); \\ \Delta Q_{rj} &= a_{j+2,1}\Delta X_o + a_{j+2,2}\Delta Y_o + \sum_{i=1, i\neq j}^{n} \left(a_{j+2,i+2}\Delta p_{ri}\right), \end{aligned} \tag{18}$$

At the next step of solution process calculated increments are added to rotor coordinates and pressures (19). Iterative process repeats until increments are higher than tolerances ε (see Fig. 3).

$$\begin{aligned} X_o^{(it+1)} &= X_o^{(it)} + \Delta X_o \; ; \\ Y_o^{(it+1)} &= Y_o^{(it)} + \Delta Y_o \; ; \\ p_{ri}^{(it+1)} &= p_{ri}^{(it)} + \Delta p_{ri}. \end{aligned} \tag{19}$$

Finally, after iterative process converged, based on the rotor equilibrium position, bearing's stiffness and damping coefficients can be determined. Stiffness and damping calculation procedure assumes that pressure in recess chambers is not changed. Stiffness coefficients are determined by following formulas:

$$k_{xx} = a_{1,1};\; k_{xy} = a_{1,2};\; k_{yx} = a_{2,1};\; k_{yy} = a_{2,2}. \tag{20}$$

For damping coefficients determination increments are added to velocities of a journal center v_x, v_y. Elrod-Adams equation (4) is solved and forces are calculated by integration (9). Damping coefficients can be found as relations (21).

$$c_{xx} = \frac{\partial F_x}{\partial v_x}, c_{xy} = \frac{\partial F_x}{\partial v_y}, c_{yx} = \frac{\partial F_y}{\partial v_x}, c_{yy} = \frac{\partial F_y}{\partial v_y}. \tag{21}$$

2. METHODOLOGY VALIDATION

Methodology validation is done through the comparison with published experimental data. The first considered case (Case #1) is based on the experimental and theoretical results published by Chaomleffel [4]. The journal bearing scheme is presented in Fig. 4a and design parameters for the analyzed journal bearing are presented in Table 1. For this case, journal load acts between recess chambers.

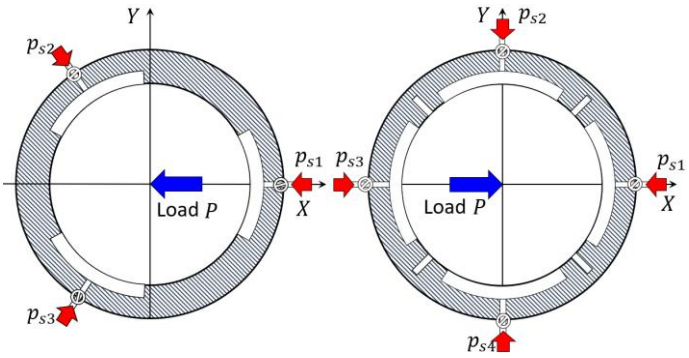

a) b)

Figure 4: Hydrostatic Bearing Scheme: a) 3 recess pockets (Case #1); b) 4 recess pockets (Case #1)

Table 1: Bearing Design Parameters (Chaomleffel)

Parameter	Symbol	Units	Value
Bearing Length	L	mm	80
Shaft Diameter	D	mm	80
Clearance (radial)	C_b	μm	125
Number of recess pockets	n	-	3
Recess length (circumferential)	$d\beta$	deg	90
Recess length (axial)	L_r	mm	50
Recess depth	h_r	mm	2
Orifice flow ratio	C_{di}	-	1
Orifice diameter	d_{oi}	mm	4.1
Rotational speed	ω	rpm	375/700/ 1500/3000
Load (along -X axis, Fig. 2a)	P	N	0-800
Pressure supply	p_{si}	MPa	0.4
Fluid viscosity	μ	$Pa\text{-}s$	0.001
Fluid density	ρ	kg/m^3	1000

Different loads and rotational speeds were considered. As an example, pressure distribution contour for the load 500 N and 3000 rpm is presented in Fig. 5.

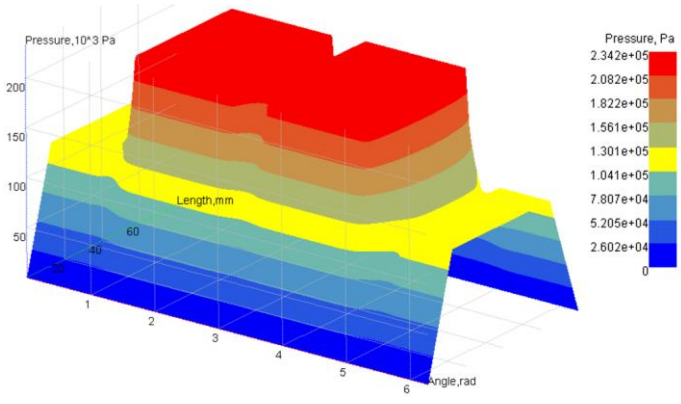

Figure 5: Pressure Distribution Contour (Case #1, 500 N, 3000 rpm)

Chart in Fig. 6 shows results of hydrostatic bearing analysis according to the proposed methodology and comparison with experiment and theoretical data from reference [4].

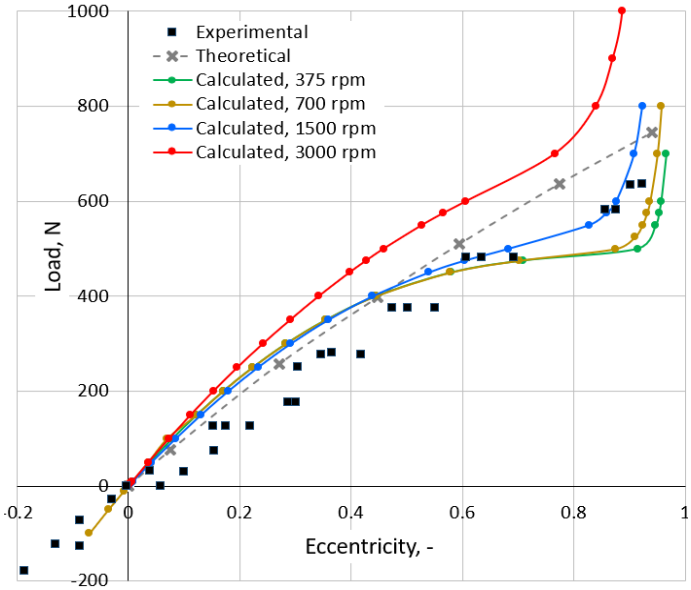

Figure 6: Load vs. Eccentricity for Calculated Results and Experiment (Case #1)

Solid lines in Fig. 6 correspond to simulation results calculated for the different shaft rotational speeds. Experimental results are shown in Fig. 6 by bar points and theoretical from [4] are indicated by grey dashed line. It should be noted that there is no information in [4] about shaft speed which was considered in the analysis.

Hydrostatic bearing eccentricity was calculated according to the approach presented in this article for small loads and matched experimental data. In the region of moderate loads (200 – 400 N) predicted eccentricities are slightly higher. For heavy loads (500 – 700 N) predicted values are close to experiment and qualitatively correspond to the experimental data pattern (curve 'distortion'). The nonlinear effect and 'distortion' of the eccentricity vs. load curve can be explained by pressure distribution profiles analysis – see Fig. 7. At comparatively low journal load the bearing operates in hydrostatic regime (Fig. 7a), while at high loads (500 – 800 N) the bearing operates in hybrid regime with hydrodynamic oil wedge, which is formed between recess chambers – see Fig. 7b.

Theoretical data presented in [4] in the region of moderate loads (200 – 400 N) matched experimental results even better than calculated in the article, but in the region of heavy loads (500 – 700 N) the effect of curve distortion is not captured (theoretical curve from [4] is almost linear).

Figure 6 also demonstrates an influence of rotational speed on hydrostatic bearing performance. Increase of rotational speed results in a decrease of eccentricity. At the speed of 3000 rpm the bearing operates in hybrid regime and eccentricity at high load becomes much smaller (almost 40% difference for 600 N load).

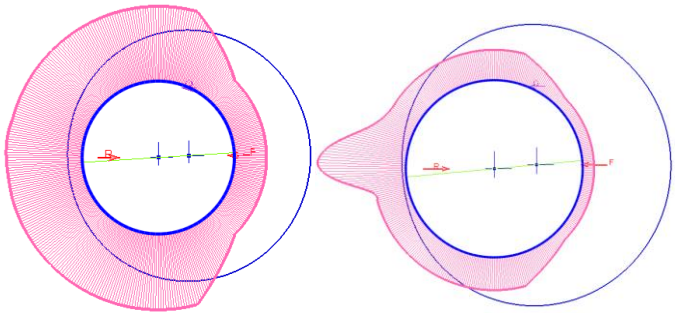

Figure 7: Pressure Distribution Profile at 1500 rpm, supply pressure 1.206 MPa and Load: a) 500 N; b) 800 N

The second example (Case #2) which was used for the methodology validation was described by San Andres in the paper [11]. The geometry of the considered bearing is presented in the scheme in Fig. 4b. Bearing parameters are presented in Table 2.

Table 2: Bearing Design Parameters (Luis San Andres)

Parameter	Symbol	Units	Value
Bearing Length	L	*mm*	53.98
Shaft Diameter	D	*mm*	114.7
Clearance (radial)	C_b	*μm*	210.8
Number of recess pockets	n	-	4
Recess length (circumferential)	$d\beta$	*deg*	56
Recess length (axial)	L_r	*mm*	35.56
Recess depth	h_r	*mm*	4.763
Orifice flow ratio	C_{di}	-	1
Orifice diameter	d_{oi}	*mm*	1.592
Rotational speed	ω	*rpm*	1000/ 2000
Load (along +X axis, Fig. 2b)	P	*N*	100
Pressure supply	p_{si}	*MPa*	1.206
Fluid viscosity	μ	*Pa-s*	0.09787
Fluid density	ρ	*kg/m³*	890

Figure 8 shows pressure distribution contour for the supply pressure 1.206 MPa, 100 N load and 1000 rpm rotational speed.

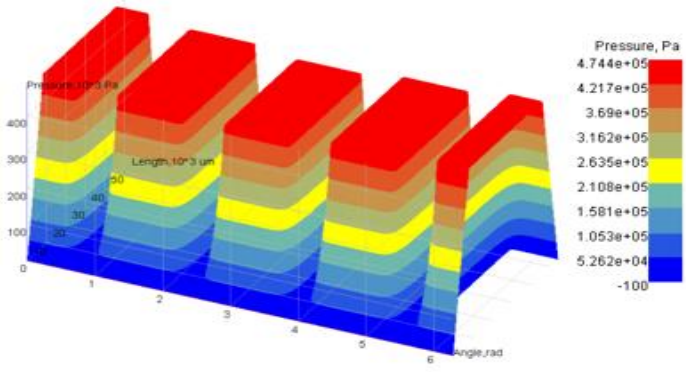

Figure 8: Pressure Distribution Contour (Case #2, 100 N, 1000 rpm)

Stiffness and damping coefficients comparisons for 1000 and 2000 rpm, 100 N load and 1.206 MPa supply pressure are presented in Fig. 9 and Fig. 10.

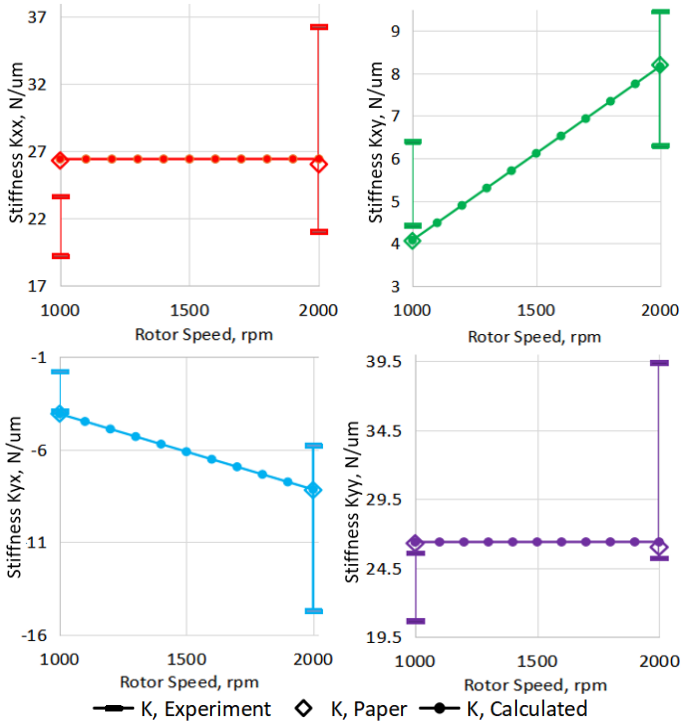

Figure 9: Bearing Stiffness (Case #2)

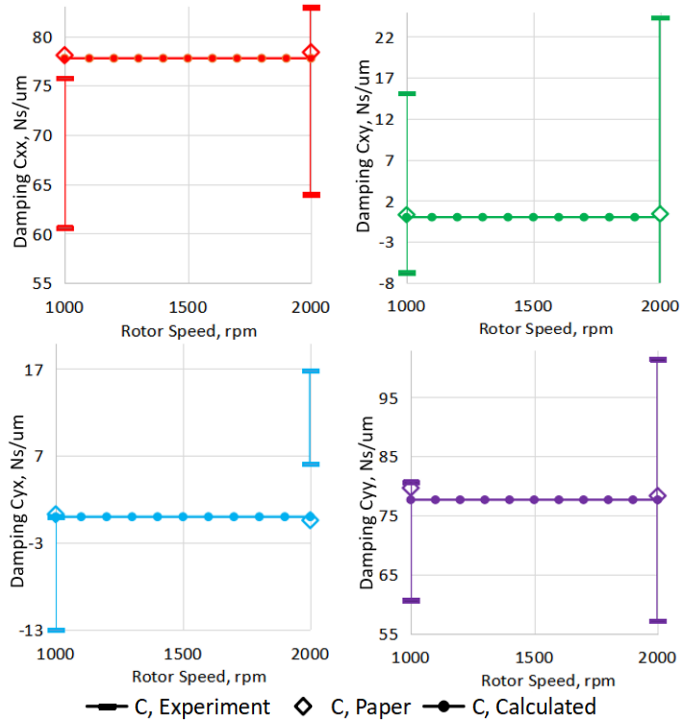

Figure 10: Bearing Damping (Case #2)

Experimental results [11] in terms of confidence interval are presented in Fig. 9, 10 by vertical lines. Theoretical results given in the article [11] are shown in Fig. 9, 10 by diamond points. Results calculated using the approach presented in this paper are shown by lines with round points in Fig. 9, 10 and agree with experimental data.

The change of the direct bearing stiffness k_{xx}, k_{yy} using approach presented in this paper and theoretical results from [11] is not significant with respect to the operating speed. Despite experimental results for k_{xx}, k_{yy} indicate some change vs. operating speed, straight horizontal lines are still possible within the confidence bars. Cross coupling stiffness k_{xy}, k_{yx} change almost linearly with respect to operating speed and reasonably well match with experimental results.

Damping coefficients c_{xx}, c_{xy}, c_{yx}, c_{yy} do not change vs. rotational speed for both sets of theoretical results. Experimentally measured damping coefficients show some difference for rotational speeds 1000 and 2000 rpm.

The comparisons between experimental and published theoretical data show that the hydrostatic bearing simulation approach gives sufficiently accurate results.

3. HYDROSTATIC BEARING INVESTIGATION

Load influence on hydrostatic bearing dynamic coefficients and parameters has been studied based on the examples from [4] and [11]. Schemes of considered bearings are presented in Fig. 4 and parameters are presented in Table 1, 2.

For the first bearing example (see Fig. 4a and Table 1) stiffness and damping coefficients were calculated for the range of loads from 0 to 800 N and shaft rotation speed 1500 rpm. Figure 6 shows a change of calculated eccentricity against applied load. Calculated direct and cross-coupled stiffness coefficients k_{xx}, k_{xy}, k_{yx}, k_{yy} are presented in Fig. 11.

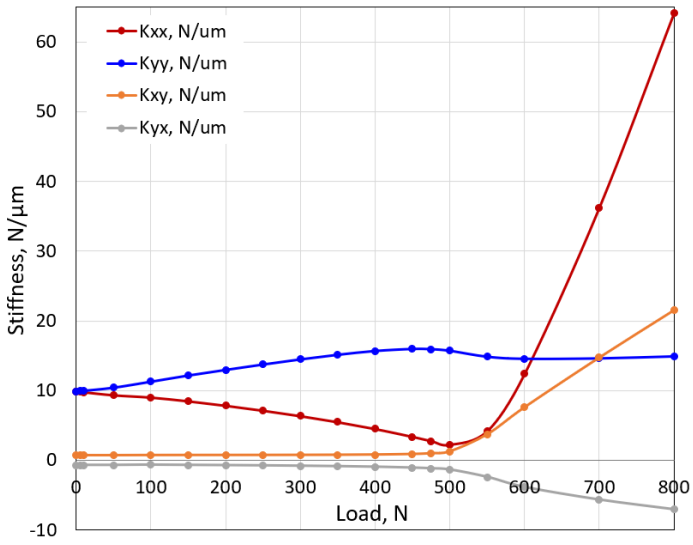

Figure 11: Stiffness Coefficients Vs. Load (Case #1)

The change of direct stiffness within hydrodynamic mode (0 – 500 N) is demonstrated in Fig. 10: k_{xx} at maximum load is more than 4 times lower, while k_{yy} at maximal load is more than 2 times higher in comparison with unloaded bearing. In the region of hybrid regime operation (>500 N), k_{xx} stiffness precipitously increases with load increase and became 6 times higher at 800 N load and 0.92 eccentricity in comparison with a not loaded case. Minimum oil film thickness falls from 39.9 µm at 500 N to 10 µm at 800 N.

A change of cross-coupled stiffness coefficients k_{xy} and k_{yx} at hydrostatic mode is about 40%. A higher change of cross-coupled stiffness coefficients is observed at loads higher 500 N and is up to 6 times at load 800 N in comparison with lightly loaded case.

Direct and cross-coupled damping coefficients c_{xx}, c_{xy}, c_{yx}, c_{yy} calculated for the same case are presented in Fig. 12.

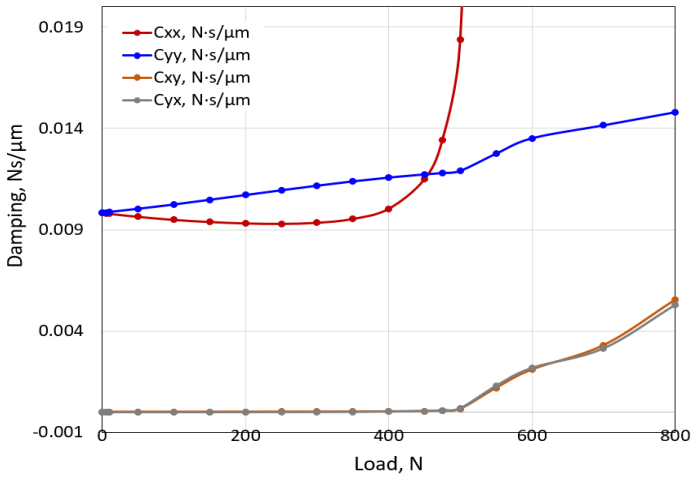

Figure 12: Stiffness Coefficients Vs. Load (Case #1)

At low loads (< 450 N) change in direct damping coefficients is not significant: variation for c_{xx} is 23% and for c_{yy} is 19%. Cross-coupled stiffness c_{xy}, c_{yx} change is not significant as coefficients remain almost constant with load increase. At high loads (500 – 800 N) c_{xx} starts to increase intensively and reaches value of 0.38 Ns/µm at 800 N load.

Second hydrodynamic bearing considered based on an example reported in [11] (Fig. 4b and Table 2). In this case journal load directs on recess chamber – see Fig. 4b. Shaft rotation speed for the considered case is 1500 rpm. Bearing hydrodynamic and mechanical parameters were calculated for the range of loads from 0 to 3000 N.

Predicted eccentricity against applied load is presented in Fig. 13. The difference in shape of the eccentricity vs. load curve for second case (Fig. 13) and the one for the first example (Fig. 6) can be explained by different load direction. It should be noted that second example of hydrostatic bearing is not able to operate with high eccentricity in hybrid regime because the journal load acts directly on the recess pocket and hydrodynamic oil wedge can't be generated.

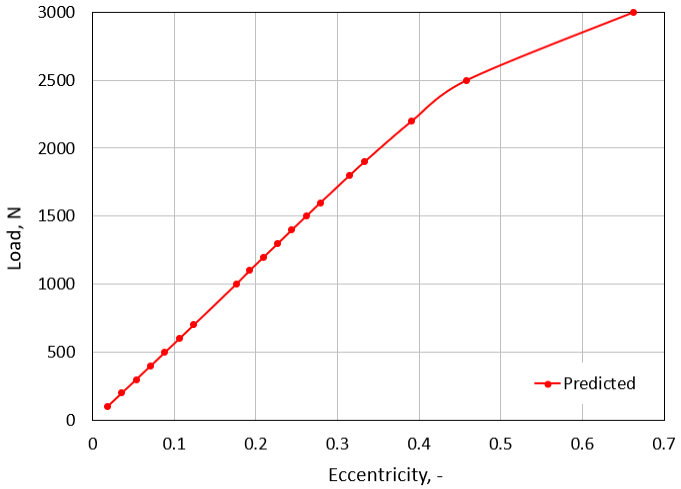

Figure 13: Eccentricity Vs. Load (Case #2)

Direct and cross-coupled stiffness coefficients k_{xx}, k_{xy}, k_{yx}, k_{yy} for the case #2 are presented in Fig. 14. It can be observed that both direct stiffnesses k_{xx} and k_{yy} in this case become lower with load increase. Cross-coupled stiffnesses coefficients k_{xy}, k_{yx} change is not significant with respect to applied journal load.

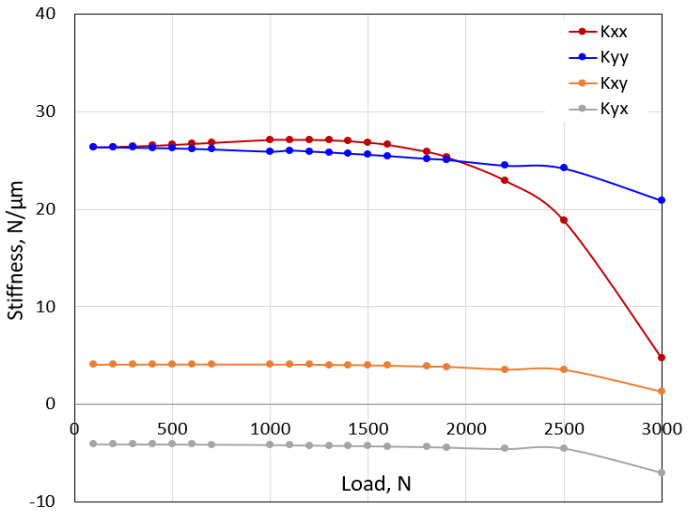

Figure 14: Stiffness Coefficients Vs. Load (Case #2)

Based on the results presented, it can be concluded that shaft eccentricity, which results from shaft load, influences hydrostatic bearing characteristics including stiffness and damping coefficients. Authors recommended to make simplifications only for the cases with small loads and eccentricities:

1) Assume rotor equilibrium position in the center of a bearing;
2) In the case of cyclically symmetric bearing, only one sector with symmetrical conditions can be considered.

The influence of eccentricity can't be ignored when comparatively high loads are applied to a journal and bearing operating in hybrid mode.

CONCLUSIONS

An approach for estimating hydrodynamical and mechanical characteristics of hybrid and hydrostatic bearings resulting in increased accuracy has been developed. The developed methodology allows estimation of the pressure and flow rates in the restrictors based on the calculated shaft equilibrium position, which depends on the applied load. Several hydrostatic bearing designs based on published data were used to validate algorithm. Comparison with experimental results and published theoretical calculations shows that the developed algorithm gives sufficiently accurate results.

The effect of load influence on the hydrodynamic and dynamic stiffness and damping characteristics has been studied. Simulation results show that eccentricity vs. load characteristics are nonlinear for the case of journal load acting between recess chambers. In the range of moderate loads, the noticeable change of dynamic coefficients takes place. In the high loaded bearings at hybrid operation modes change of bearing stiffness and damping is significant and can't be ignored.

Results of this study show that for loaded bearings, shaft eccentricity must be taken into consideration as it influences hydrostatic bearing performance characteristics as well as stiffness and damping coefficients.

REFERENCES

[1] Liu, Z. A., Wang, Y., Cai, L., Zhao, Y., Cheng. Q. Dong, X., 2017, "Review of Hydrostatic Bearing System Recearches and Applications," Advances in Mechanical Engineering, 9(10), pp. 1-27.

[2] Guo, Z., Hirano, T., Kirk, R.G., 2015, "Application of CFD Analysis for Rotating Machinery - Part I: Hydrodynamic, Hydrostatic Bearings and Squeeze Film Damper," Journal of Engineering for Gas Turbines and Power, 127, pp 445-451.

[3] Kishor S., 2016, 'Numerical Modeling and Simulation of Viscous Shear in Hydrostatic Bearing," Proceeding of ASME 2016 Power Conference, Charlotte, North Carolina, ASME Paper No. POWER2016-59410.

[4] Chaomleffel, J.P., Nicolast, D., 1986, "Experimental investigation of hybrid journal bearings," Tribology International, 19(5), pp. 253-259.

[5] Constantinescu, V.N., Galutuse, S. and Kennedy, F., 2016, "On the comparison between lubrication theory, including turbulence and inertia forces, and some existing experimental data," Trans. ASMEJolt, 1975, pp. 439-449.

[6] Wang N., Cha K, Huang H., 2012, 'Fast Convergence of Iterative Computation for Incompressible-Fluid Reynolds Equation,' ASME J. Tribol, 134(2).

[7] Sharma, S.C., Phalle, V.M., Jain, S.C., 2011, "Performance analysis of a multirecess capillary compensated conical hydrostatic journal bearing", Tribology International, 44, pp. 617-626.

[8] Elrod, H.G., Adams, M., 1974, “A computer program for cavitation and starvation problems. Technical report 190.” 1st LEEDS LYON Symposium on Cavitation and Related Phenomena in Lubrication, I.M.E., 103, pp. 37-41.
[9] Moroz, L., Romanenko, L., Kochurov, R., Kashtanov, E., 2018, “Hydrodynamic Journal Bearings Optimization Considering Rotor Dynamics Restrictions,” Proccedings of ASME Turbo Expo 2018, Oslo, Norway, ASME Paper No. GT2018-75790.
[10] Szeri, A.Z., 2011, Fluid Film Lubrication. Second Edition. Cambridge University Press, New York.
[11] San Andres, L., 1993, “Thermohydrodynamic Analysis of Cryogenic Liquid Turbulent Flow Fluid Film Bearings,” Technical Report to NASA Lewis Research Center, NASA Grant NAG3-1434.
[12] Childs D., Hale K., 1994, “A Test Apparatus and Facility to identify the Rotordynamic Coefficients of High-Speed Hydrostatic Bearings,” ASME J. Tribol, 116, p.343.